

Studies of granularity of a hadronic calorimeter for tens-of-TeV jets at a 100 TeV pp collider

Chih-Hsiang Yeh^e, S.V. Chekanov^a, A.V. Kotwal^{b,c}, J. Proudfoot^a, S. Sen^b,
N.V. Tran^c, S.-S. Yu^e

^a *HEP Division, Argonne National Laboratory, 9700 S. Cass Avenue, Argonne, IL 60439, USA.*

^b *Department of Physics, Duke University, USA*

^c *Fermi National Accelerator Laboratory*

^d *Department of Physics, Michigan State University, 220 Trowbridge Road, East Lansing, MI 48824*

^e *Department of Physics, National Central University, Chung-Li, Taoyuan City 32001, Taiwan*

Abstract

Jet substructure of hadronic jets with transverse momenta in the range from 2.5 TeV to 20 TeV were studied using several designs for spacial size of calorimeter cells. The studies using full simulation of calorimeter response complimented with the reconstruction of calorimeter clusters for jet reconstruction. The results unambiguously indicate that performance of jet substructure reconstruction improves with reducing the cell sizes.

Keywords: multi-TeV physics, pp collider, future hadron colliders, FCC, SppC

1. Introduction

Particle collisions at energies beyond those attained at the LHC will lead to many challenges for detector technologies. Future experiments, such as high-energy LHC (HE-LHC), future circular pp colliders of the European initiative, FCC-hh [1] and the Chinese initiative, SppC [2] will be required to measure high-momentum bosons (W , Z , H) and top quarks with strongly collimated decay products that form jets. Studies of jet substructure can help identify such particles.

The reconstruction of jet substructure variables for collimated jets with transverse momentum above 10 TeV require an appropriate detector design. The most important for reconstruction of such jets are tracking and calorimeter. Recently, a number of studies [3, 4, 5] have been discussed using various fast simulation tools, such as Delphes [6], in which momenta of particles are smeared to mimic detector response.

A major step towards the usage of full Geant4 simulation to verify the granularity requirements for calorimeters was made in [7]. The studies included in this paper have illustrated a significant impact of granularity of electromagnetic (ECAL) and hadronic (HCAL) calorimeters on the shape of hadronic showers calculated using calorimeter

Email addresses: chekanov@anl.gov (S.V. Chekanov), ashutosh.kotwal@duke.edu (A.V. Kotwal), proudfoot@anl.gov (J. Proudfoot), sourav.sen@duke.edu (S. Sen), ntran@fnal.gov (N.V. Tran), syu@cern.ch (S.-S. Yu), jwzuzelski18@gmail.com (Chih-Hsiang Yeh)

hits for two particles separated by some angle. It was concluded that high granularity is essential in resolving two close-by particles for energies above 100 GeV.

This paper makes another step in understanding of this problem in terms of high-level physics quantities typically used in physics analyses. Similar to the studies presented in [7], this paper is based on a full Geant4 simulation with realistic jet reconstruction.

2. Simulation of detector response and event reconstruction

The description of the detector and software used for this paper is discussed in [7]. We use the SiFCC detector geometry with a software package that represents a versatile environment for simulations of detector performance, testing new technology options, event reconstruction techniques for future 100 TeV colliders.

The GEANT4 (version 10.3) [8] simulation of calorimeter response was complemented with the full reconstruction of calorimeter clusters formed by the Pandora algorithm [9, 10]. Calorimeter clusters were built from calorimeter hits in the ECAL and HCAL after applying the corresponding sampling fractions. No other corrections are applied. Hadronic jets were reconstructed with the FASTJET package [11] using the anti- k_T algorithm [12] with a distance parameter of 0.5.

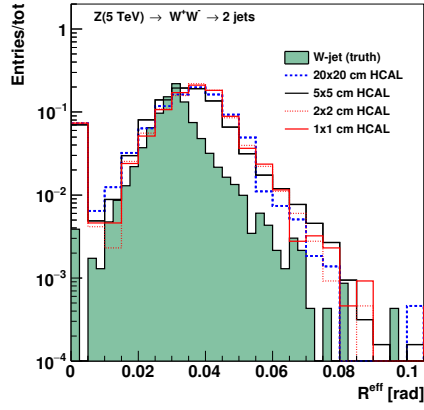
In the following discussion, we use the simulations of a heavy Z' boson, a hypothetical gauge boson that arises from extensions of the electroweak symmetry of the Standard Model. The Z' bosons were simulated with the masses, $M = 5, 10, 20$ and 40 TeV. The lowest value represents a typical mass that is within the reach of the LHC experiments. The value 40 TeV represents the physics reach for a 100 TeV collider. The Z' particles are forced to decay to two light-flavor jets ($q\bar{q}$), W^+W^- or $t\bar{t}$, where W and t decay hadronically. In all such scenarios, two highly boosted jets are produced, which are typically back-to-back in the laboratory frame. Typical transverse momenta of such jets are $\simeq M/2$. The main difference between considered decay types lays in different jet substructure. In the case of the $q\bar{q}$ decays, jets do not have any internal structure. In the case of W^+W^- , each jet originates from W , thus it has two subjects because of the decay $W \rightarrow q\bar{q}$. In the case of hadronic top decays, jets have three subjects due to the decay $t \rightarrow W^+b \rightarrow q\bar{q}b$. The signal events were generated using the PYTHIA8generator with the default settings, ignoring interference with SM processes. The event samples used in this paper are available from the HepSim database [13].

3. Studies of jet properties

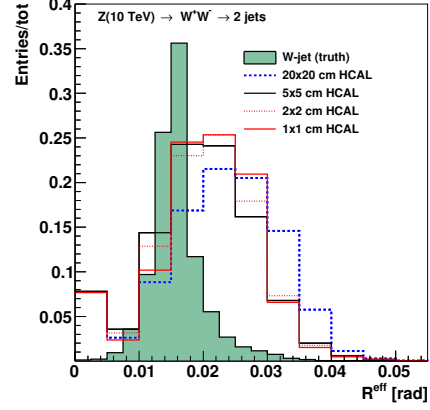
First let us consider several variables that represent jet substructure using different types of calorimeter granularity. The question we want to answer is how close the reconstructed jet substructure variables to the input "truth" value that are reconstructed using input particles directly from the PYTHIA8generator.

The effective radius is the average of the energy weighted radial distance in $\eta - \phi$ space of jet constituents. Recently, it has been studied for multi-TeV jets in Ref.[14].

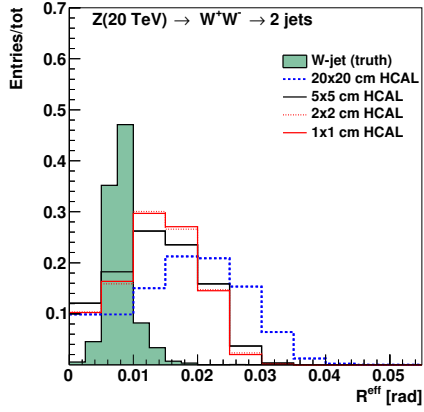
Let us study the effect of granularity on jet splitting scales. A jet k_T splitting scale [15] is defined as a distance measure used to form jets by the k_T recombination algorithm [16, 17]. This has been studied by ATLAS [18], and more recently in the context of 100



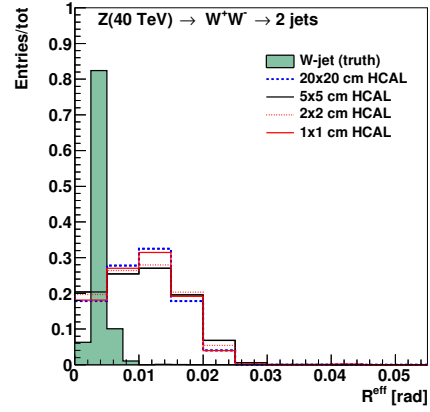
(a) 5 TeV



(b) 10 TeV



(c) 20 TeV



(d) 40 TeV

Figure 1: Jet effective radius for different jet transverse momenta and HCAL granularities.

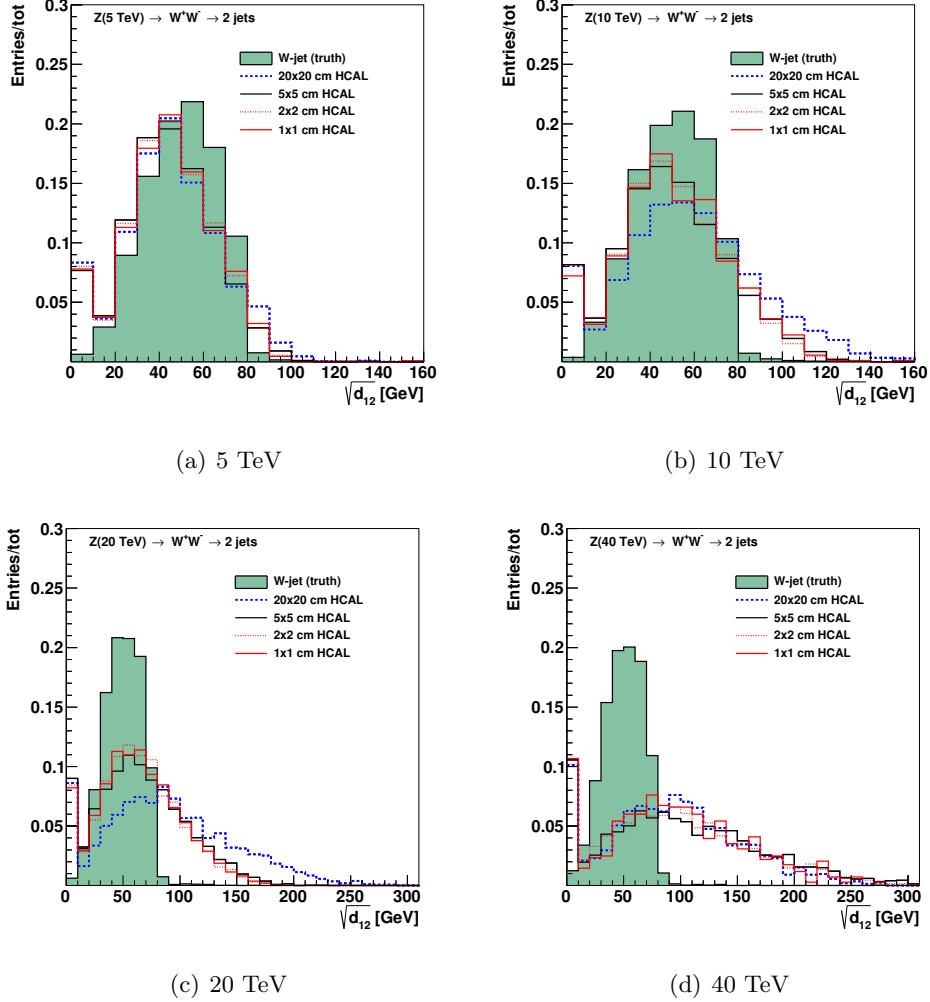


Figure 2: Jet splitting scale for different jet transverse momenta and HCAL granularity.

TeV physics [14]. The distribution of the splitting scale $\sqrt{d_{12}} = \min(p_T^1, p_T^2) \times \delta R_{12}$ [18] at the final stage of the k_T clustering, where two subjets are merged into the final one, is shown in Fig. 2.

3.1. Jet subjettiness

We recall that N -subjettiness [19], τ_N , of jets has been proposed as a class of variables with which to study the decay products of a heavy particle inside jets. τ_N is a measure of the degree to which a jet can be considered as being composed of N k_T -subjets [19]. The variable τ_{32} , defined as the ratio of the N -subjettiness variables τ_3/τ_2 , is particularly sensitive to hadronically-decaying top-quark initiated jets. The variable, $\tau_{21} \equiv \tau_2/\tau_1$ can be used to reject background from W/Z decays. These variables do not strongly correlate with jet mass and can provide an independent check for the presence of top quarks. The jet substructure variables were obtained by re-running the

71 k_T algorithm over the jet constituents of anti- k_T jets.

72 4. Study of detector performance with soft drop mass

73 In this section, we use the jet mass computed with a specific algorithm, soft drop
74 declustering, to study the performance of detector with various detector cell sizes and
75 center-of-mass (c.m.) energies.

76 4.1. The technique of soft drop declustering

77 The soft drop declustering [?] is a grooming method that removes soft wide-
78 angle radiation from a jet. The constituents of a jet j_0 are first reclustered using the
79 Cambridge-Aachen (C/A) algorithm [? ?]. Then, the jet j_0 is broken into two subjets
80 j_1 and j_2 by undoing the last stage of C/A clustering. If the subjets pass the following
81 soft drop condition, jet j_0 is the final soft-drop jet. Otherwise, the algorithm redefines
82 j_0 to be the subjet with larger p_T (among j_1 and j_2) and iterates the procedure.

$$\frac{\min(p_{T1}, p_{T2})}{p_{T1} + p_{T2}} > z_{\text{cut}} \left(\frac{\Delta R_{12}}{R_0} \right)^\beta, \quad (1)$$

83 where p_{T1} and p_{T2} are the transverse momenta of the two subjets, z_{cut} is soft drop
84 threshold, ΔR_{12} is the distance between the two subjets in the η - ϕ plane, R_0 is the
85 characteristic radius of the original jet, and β is the angular exponent.

86 In our study, we compare the performance of future detector when setting $\beta = 0$
87 versus when setting $\beta = 2$. For $\beta = 0$, the soft drop condition depends only on the z_{cut} .
88 For $\beta = 2$, the condition depends on the angular distance between the two subjets and
89 z_{cut} and the algorithm becomes infrared and collinear safe.

90 4.2. Analysis method

91 We employ the following method to quantify the detector performance and find out
92 the cell size that gives the best separation power to distinguish signal from background.
93 For each configuration of detector and c.m. energy, we draw the receiver operating
94 characteristic (ROC) curves in which the x-axis is the signal efficiency (ϵ_{sig}) and y-axis
95 is the inverse of background efficiency ($1/\epsilon_{\text{bkg}}$). In order to scan the efficiencies of soft
96 drop mass cuts, we vary the mass window as follows. We first look for the median
97 bin i_{med} ¹ of the soft drop mass histogram from simulated signal events. Taking the
98 right boundary of bin i_{med} as the center of mass window x_{center} , we start increasing the
99 width of mass window symmetrically on the left and on the right of x_{center} , in steps of
100 5 GeV, i.e. the narrowest mass window is $[x_{\text{center}} - 5, x_{\text{center}} + 5]$. If one side reaches
101 the boundary of the mass histogram, we only increase the width on the other side, also
102 in steps of 5 GeV. For each mass window, there will be corresponding ϵ_{sig} and ϵ_{bkg} ,
103 which gives a point in the ROC curves.

¹The integral from bin 0 to bin i_{med} ($i_{\text{med}} - 1$) should be greater (less) than half of the total number of events. Note, the bin width is 5 GeV.

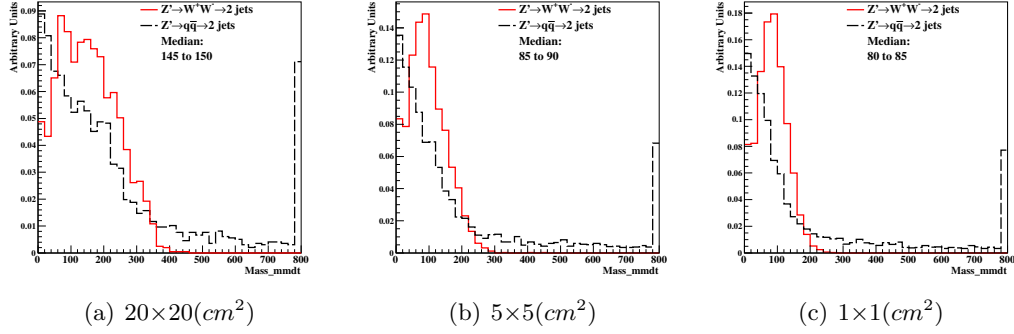


Figure 3: Distributions of soft drop mass for $\beta=0$, with 20 TeV c.m. energies and three different detector cell sizes: 20×20 , 5×5 , and 1×1 (cm^2). The signal (background) process is $Z' \rightarrow WW$ ($Z' \rightarrow q\bar{q}$).

4.3. Results and conclusion

Figures 3, 5, 7, and 9 present the distributions of soft drop mass for $\beta = 0$ and $\beta = 2$ with different c.m. energies and detector cell sizes; the signals considered are $Z' \rightarrow WW$ and $Z' \rightarrow t\bar{t}$. In Figs. 4, 6, 8, and 10, ROC curves from different detector cell sizes are compared for each c.m. energy, respectively.

Figures 4 and 6 show that for $\beta = 0$ the smallest detector cell size, $1 \text{ cm} \times 1 \text{ cm}$, has the best separation power at $\sqrt{s} = 5, 10$, and 20 TeV when the signal is $Z' \rightarrow WW$ and at $\sqrt{s} = 10$ and 20 TeV when the signal is $Z' \rightarrow t\bar{t}$. On the contrary, Figs. 8 and 10 show that for $\beta = 2$ the smallest detector cell size does not have improvements in the separation power with respect to those with larger cell sizes. In fact, the performances of the three cell sizes are similar. In addition, sometimes bigger detector cell sizes, $5 \text{ cm} \times 5 \text{ cm}$ or $20 \text{ cm} \times 20 \text{ cm}$ have the best separation power.

We also find compared to $\beta = 2$, soft drop mass with $\beta = 0$ has better performance for distinguishing signal from background. Therefore, we will apply requirements on this variable when studying the other jet substructure variables.

5. Study of detector performance with jet substructure variables

In this section, we use the different jet substructure variables to study the performance of detector with various detector cell sizes and c.m. energies.

5.1. N-subjettiness

N-subjettiness[??] is the detection technique of jet substructure that is employed to identify boosted hadronically-decaying objects under the high c.m. energies conditions. We apply τ variables to distinguish the number of subjet(s) in a large radius ($R=0.4$) jets to separate signal from background with various detector cell sizes and c.m. energies.

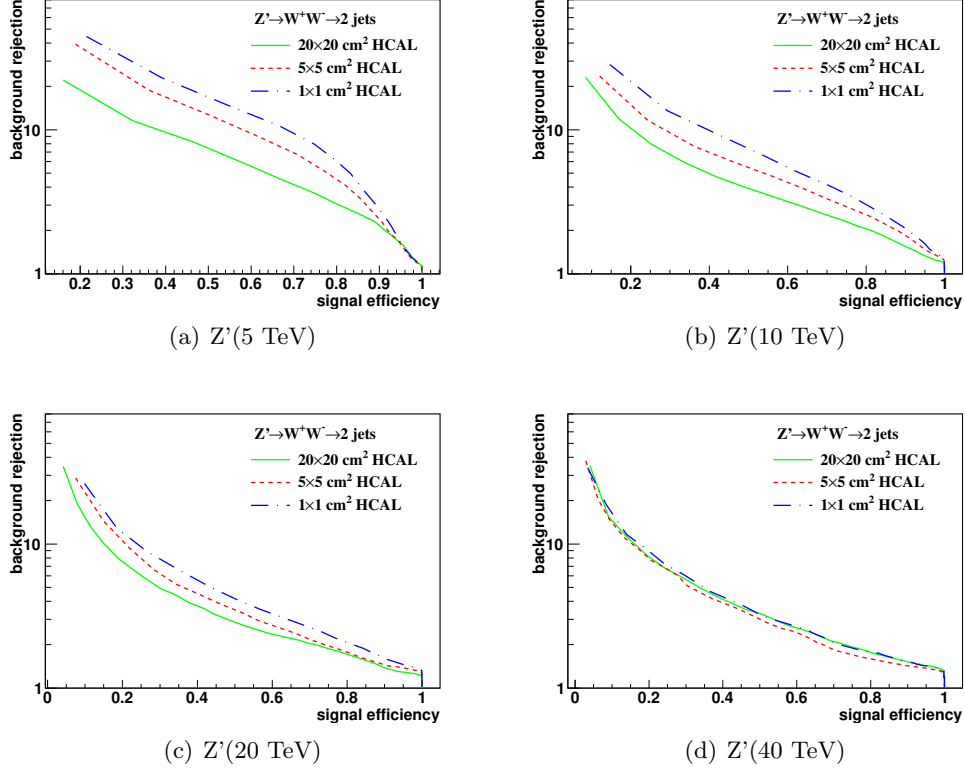


Figure 4: The ROC curves of soft drop mass selection for $\beta=0$ with 5, 10, 20, 40 TeV c.m. energies. Three different detector cell sizes are compared: 20×20 , 5×5 , and $1 \times 1 \text{ (cm}^2\text{)}$. The signal (background) process is $Z' \rightarrow WW$ ($Z' \rightarrow q\bar{q}$).

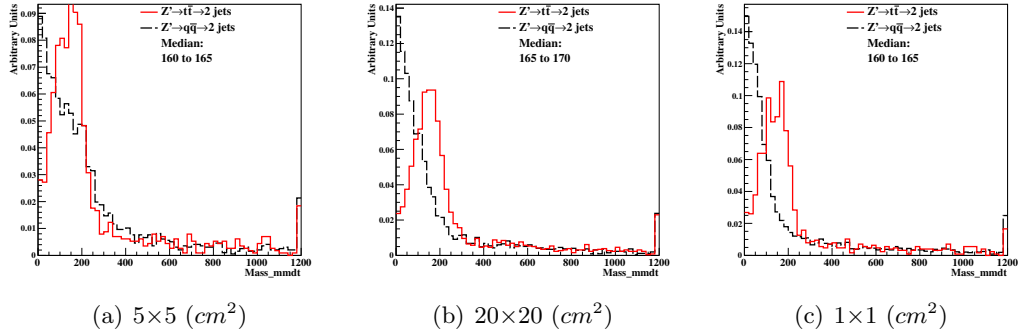


Figure 5: Distributions of soft drop mass for $\beta=0$, with 20 TeV c.m. energies and three different detector cell sizes: 20×20 , 5×5 , and $1 \times 1 \text{ (cm}^2\text{)}$. The signal (background) process is $Z' \rightarrow t\bar{t}$ ($Z' \rightarrow q\bar{q}$).

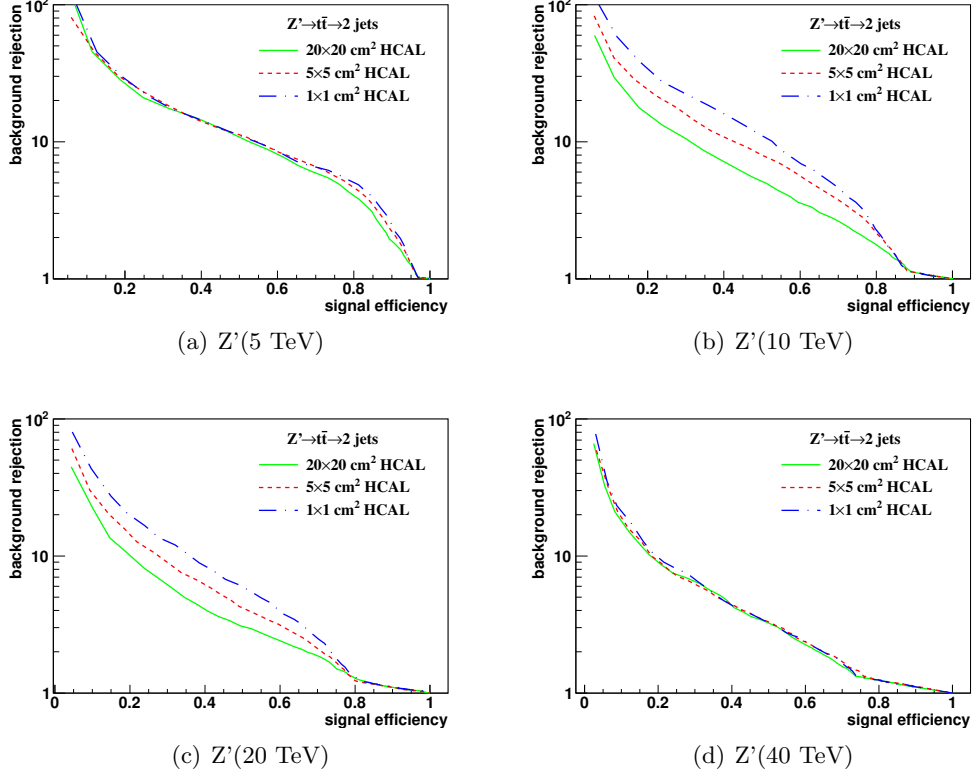


Figure 6: The ROC curves of soft drop mass selection for $\beta=0$ with 5,10, 20, 40 TeV c.m. energies. Three different detector cell sizes are compared: 20×20 , 5×5 , and 1×1 (cm^2). The signal (background) process is $Z' \rightarrow t\bar{t}$ ($Z' \rightarrow q\bar{q}$).

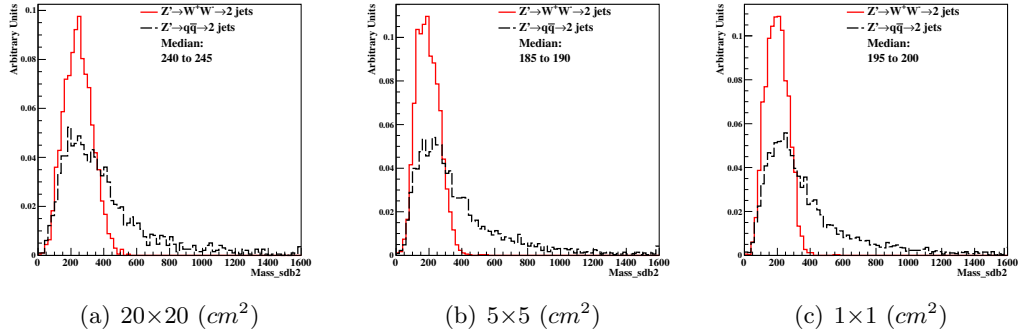


Figure 7: Distributions of soft drop mass for $\beta=2$, with 20 TeV c.m. energies and three different detector cell sizes: 20×20 , 5×5 , and 1×1 (cm^2). The signal (background) process is $Z' \rightarrow WW$ ($Z' \rightarrow q\bar{q}$).

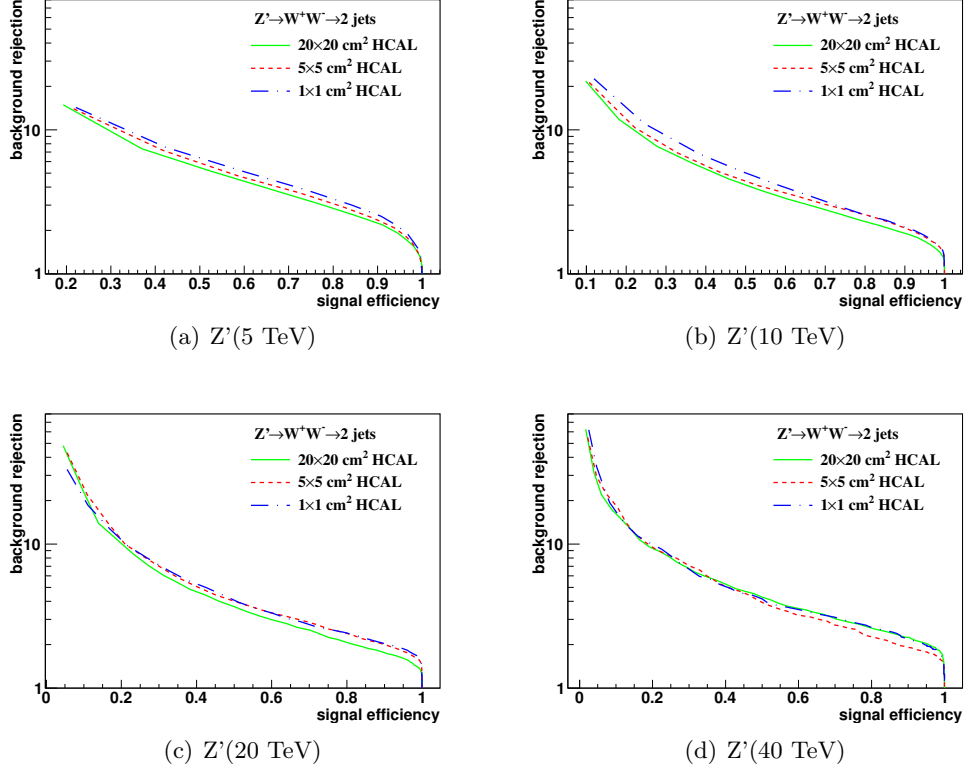


Figure 8: The ROC curves of soft drop mass selection for $\beta=2$ with 5, 10, 20, 40 TeV c.m. energies. Three different detector cell sizes are compared: 20×20 , 5×5 , and 1×1 (cm^2). The signal (background) process is $Z' \rightarrow WW$ ($Z' \rightarrow q\bar{q}$).

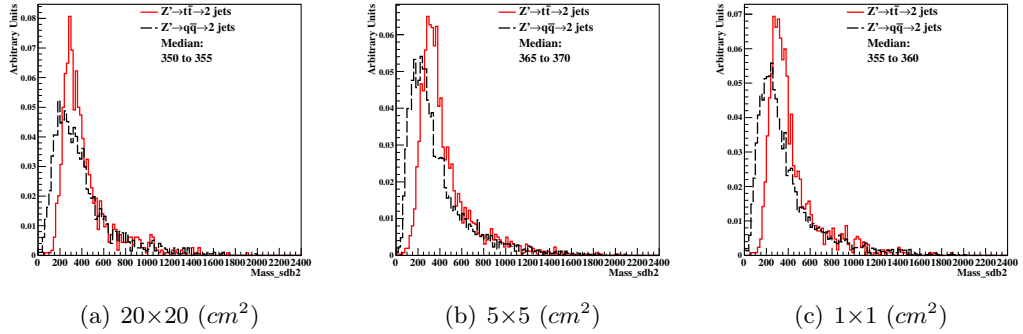
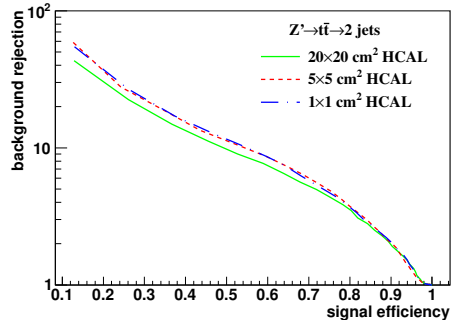
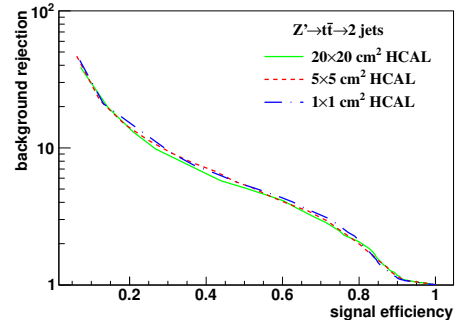


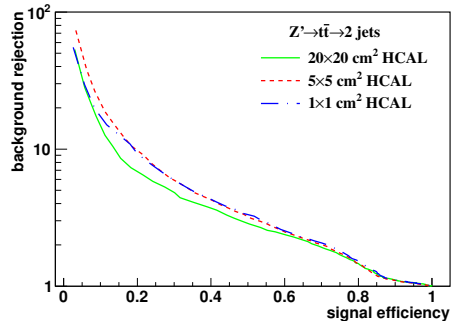
Figure 9: Distributions of soft drop mass for $\beta=2$, with 20 TeV c.m. energies and three different detector cell sizes: 20×20 , 5×5 , and 1×1 (cm^2). The signal (background) process is $Z' \rightarrow t\bar{t}$ ($Z' \rightarrow q\bar{q}$).



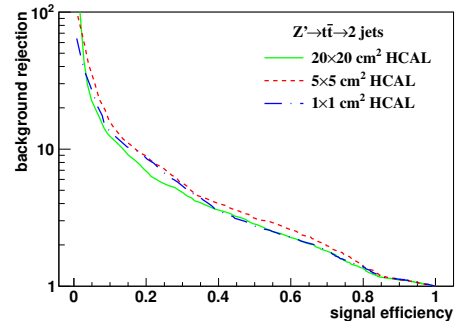
(a) $Z' (5 \text{ TeV})$



(b) $Z' (10 \text{ TeV})$



(c) $Z' (20 \text{ TeV})$



(d) $Z' (40 \text{ TeV})$

Figure 10: The ROC curves of soft drop mass selection for $\beta=2$ with 5, 10, 20, 40 TeV c.m. energies. Three different detector cell sizes are compared: 20×20 , 5×5 , and $1 \times 1 \text{ (cm}^2\text{)}$. The signal (background) process is $Z' \rightarrow t\bar{t}$ ($Z' \rightarrow q\bar{q}$).

5.1.1. The technique of N -subjettiness

The N -subjettiness is the method that can distinguish different number of subjects in a large radius jet. Anti-kt(AK4) algorithm is first used to reconstruct jets. Then, after reconstructing, exclusive k_T algorithm[??] is applied in finding the jet axis in a large radius jet. Next, start running formula and loop all constituent particles in a large radius jet. In the end, it will give out the positive integer τ_N . If a large radius jet has N subjet(s)[??], its τ_N is smaller than other number of subjects τ_N . Therefore, we define the ratio of τ_N variable, $\tau_{21}(=\frac{\tau_2}{\tau_1})$ and $\tau_{32}(=\frac{\tau_3}{\tau_2})$, and employing them to study the subjet(s) numbers in a large radius jet.

$$\tau_N = \frac{1}{d_0} \sum_k p_{T,k} \min\{\Delta R_{1,k}, \Delta R_{2,k}, \dots, \Delta R_{N,k}\} \quad (2)$$

$$d_0 = \sum_k p_{T,k} R_0 \quad (3)$$

k runs over all constituent particles in the given the large radius jet, $p_{T,k}$ are their transverse momentum, $\Delta R_{J,k} = \sqrt{(\Delta\eta)^2 + (\Delta\phi)^2}$ is the distance between the constituent particles k and the candidate subjet J on the $\eta - \phi$ plane. R_0 is the characteristic jet radius used in Anti-kt(AK) jet algorithm at starting. d_0 is the normalization factor.

In our study, we compare the performance of detector with τ_{21} and τ_{32} , and see whether they can distinguish two-prong jets and three-prong jets from one-prong jet individually with various detector cell sizes and c.m. energies.

5.1.2. Analysis method

We apply the following way to quantify the detector performance and figure out the cell size that gives the best separation power to distinguish signal from background. For each configuration of detector and c.m. energy, we employ ROC curves, same as soft drop mass ROC curves plots. For scanning the efficiencies of ratio of τ variables, we use the different width of window. First, suggested by the paper[??], we apply the mass cut before we draw the ROC curves. We look for the median bin of the soft drop mass with $\beta = 0$ histogram from simulated signal events. Then, compare left and right bin content, and add the higher side to be the new mass window. When we compare to the window that includes 75% of total signal mass, we will stop and use the events include the latest window.

Next, we will use those events to draw the ROC curves. From the pearson lemma, it tells us that uses the ratio histograms to be the ROC curves window reference, and it will give us the best ROC curves. So we use this method to do the analysis. We plot out the ratio histograms, and find out the maximum bin to be our seed bin. This is the first window. Then, we compare the left and right ratio histogram bin content, and add the higher side to be our next window. In every window, it will have the corresponding ϵ_{sig} and $1/\epsilon_{\text{bkg}}$ efficiency. In the end, it will give out the ROC curves.

For another method to quantify the detector performance, we use the "Mann-Whitney" test to do. In the figure 17(a), it shows the Mann-Whitney values that are computed with various detector cell sizes and c.m. energies. By the definition of

the Mann-Whitney value, if the value of it is bigger, that means the two distributions have the similar components. On the other hand, it means we can't separate signal from background very well. From another point of view, if the value of it is smaller, that means we can separate signal from background well.

5.1.3. The results and conclusion

Figures 13,15 show the histograms of τ_{21} and τ_{32} $\sqrt{s}=20$ TeV after cutting the mass variable. The signals considered are $Z'\rightarrow WW$ (τ_{21}) and $Z'\rightarrow t\bar{t}$ (τ_{32}). In figure 14,16, they present the ROC curves from different detector cell sizes are compared for each c.m. energy, respectively.

As a result of figure 14, 16, they perform the ROC curves of τ_{21} and τ_{32} with different detector cell sizes and c.m. energy. The smallest detector cell (1×1 cm²) doesn't have the best separation power to distinguish signal from background. Some of them have the best separation power with the bigger cell size (5×5 cm² and 20×20 cm²).

In Figure 17(a)(b), they present the summary plots of τ_{21} and τ_{32} with various detector cell sizes and c.m. energies using Mann Whitney U test. For τ_{21} , $\sqrt{s}=5$ has better separation power when detector sizes get smaller. When c.m. energy increases, there is no improvement in the smallest detector cell size (1×1 cm²). For τ_{32} , the case is similar to τ_{21} . Even worse, with some c.m. energies, the bigger detector cell sizes (5×5 cm² and 20×20 cm²) have better separation power than the smallest detector sizes (1×1 cm²).

5.2. Studies of signal and background separation using jet substructure variable: Energy correlation function

Energy correlation function (ECF) [??] is another kind of detection technique of jet substructure that is applied to distinguish the number of subjets in a large radius jet under high c.m. energy conditions. We employ ECF to separate signal from background with various detector cell sizes and c.m. energies. In Figure [17](a)(b), they show the summary plots of τ_{21} and τ_{32} with the rawhit cut with 0.5GeV using Mann Whitney U test. In τ_{21} , 5TeV has better separation power when detector sizes get smaller. When energy increases, there is no improvement in the smallest detector cell size (1×1). In τ_{32} , the case is similar to τ_{21} . Even worse, with some c.m. energies, the bigger detector sizes (5×5 and 20×20) have better separation power than the smallest detector sizes (1×1).

5.3. Studies of signal and background separation using jet substructure variable: Energy correlation function

Energy correlation function (ECF) [??] is another kind of detection technique of jet substructure that is used to distinguish the number of subjets in a fatjet under high c.m. energy conditions. This method only uses the momenta of particles and the angles between them without additional algorithm.

5.3.1. The technic of energy correlation function

The energy correlation function is another the method that can distinguish different number of subjets in a large radius jet. This method is only applied the momenta of

particles and the angles between the particles without additional algorithm. In the formula 4, the sum loop all particles in the jet J , E are the energy of particles, and θ are the angles between the particles

$$ECF(N, \beta) = \sum_{i_1 < i_2 < \dots < i_N \in J} \left(\prod_{a=1}^N E_{ia} \right) \left(\prod_{b=1}^{N-1} \prod_{c=b+1}^N \theta_{i_b i_c} \right)^\beta \quad (4)$$

We apply two approximation. First, because under the high energy limitation $p \gg m$, $E \approx p$. Second, we use Radius R between particles naturally, so our ECF formula (4) can be modified to the formula(5). From the modified ECF formula (5), in order to use the dimensionless observation to determine whether the number of subjets in system, parameter τ_N is defined as formula (6)

$$ECF(N, \beta) = \sum_{i_1 < i_2 < \dots < i_N \in J} \left(\prod_{a=1}^N P_{ia} \right) \left(\prod_{b=1}^{N-1} \prod_{c=b+1}^N R_{i_b i_c} \right)^\beta \quad (5)$$

$$\tau_N^{(\beta)} \equiv \frac{ECF(N+1, \beta)}{ECF(N, \beta)} \quad (6)$$

The idea of formula (6) is from N-subjetness, because the behavior of it is very similar to N-subjetness as reference [??]. In general, if the system has N subjets, $ECF(N+1, \beta)$ should be significantly smaller than $ECF(N, \beta)$, so we can use this advantage to distinguish different number of subjets. Finally, because it is suggested by using τ_{21} , τ_{32} [??] to distinguish two-prong jets and three-prong jets from one-prong jet, in the ECF, it also defines the ratio of τ there, and define the energy correlation double ratio that is used in our study:

$$C_N^{(\beta)} \equiv \frac{\tau_N^{(\beta)}}{\tau_{N-1}^{(\beta)}} = \frac{ECF(N-1, \beta) ECF(N+1, \beta)}{ECF(N, \beta)^2} \quad (7)$$

In our study, We set $N=2$ and $\beta = 1$ (C_2^1) and see whether they can distinguish two-prong jets from one-prong jet individually with various detector cell sizes and c.m. energies.

5.3.2. Analysis method

Same as 5.1.2.

5.3.3. The results and conclusion

In the figure 11, they present the histograms of C_2^1 with $\sqrt{s}=20$ TeV after cutting the mass variable. The signals considered are $Z' \rightarrow WW$. In figure 12, it presents the ROC curves from different detector cell sizes are compared for each c.m. energy, respectively. As a result of figure 12, it performs the ROC curves of C_2^1 with different detector cell sizes and c.m. energy. The smallest detector cell (1×1 cm²) doesn't have the best separation power to distinguish signal from background. In addition, in some cases such like (a), the biggest one (20×20 cm²) has the best distinguish power under the same c.m. energy. In Figure 17(c), it presents the summary plots of C_2^1 with the

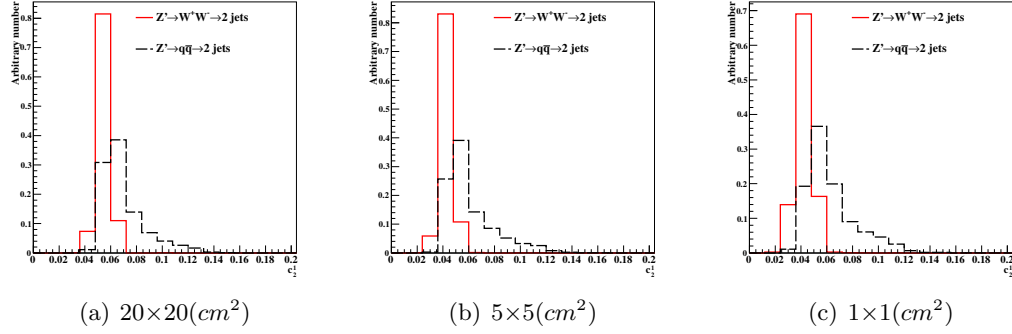


Figure 11: Distributions of Mann-Whitney value U in 20 TeV energy collision for C_2^1 in different detector sizes. Cell Size in 20×20 , 5×5 , and $1 \times 1 (cm \times cm)$ are shown here.

247 0.5GeV rawhit cut applying Mann Whitney U test. When c.m. energy increases, there
 248 is no improvement in the smallest detector cell size ($1 \times 1 cm^2$) for all c.m. energies.

249 Acknowledgements

250 This research was performed using resources provided by the Open Science Grid,
 251 which is supported by the National Science Foundation and the U.S. Department of
 252 Energy's Office of Science. We gratefully acknowledge the computing resources provided
 253 on Blues, a high-performance computing cluster operated by the Laboratory Computing
 254 Resource Center at Argonne National Laboratory. Argonne National Laboratory's work
 255 was supported by the U.S. Department of Energy, Office of Science under contract DE-
 256 AC02-06CH11357. The Fermi National Accelerator Laboratory (Fermilab) is operated
 257 by Fermi Research Alliance, LLC under Contract No. DE-AC02-07CH11359 with the
 258 United States Department of Energy.

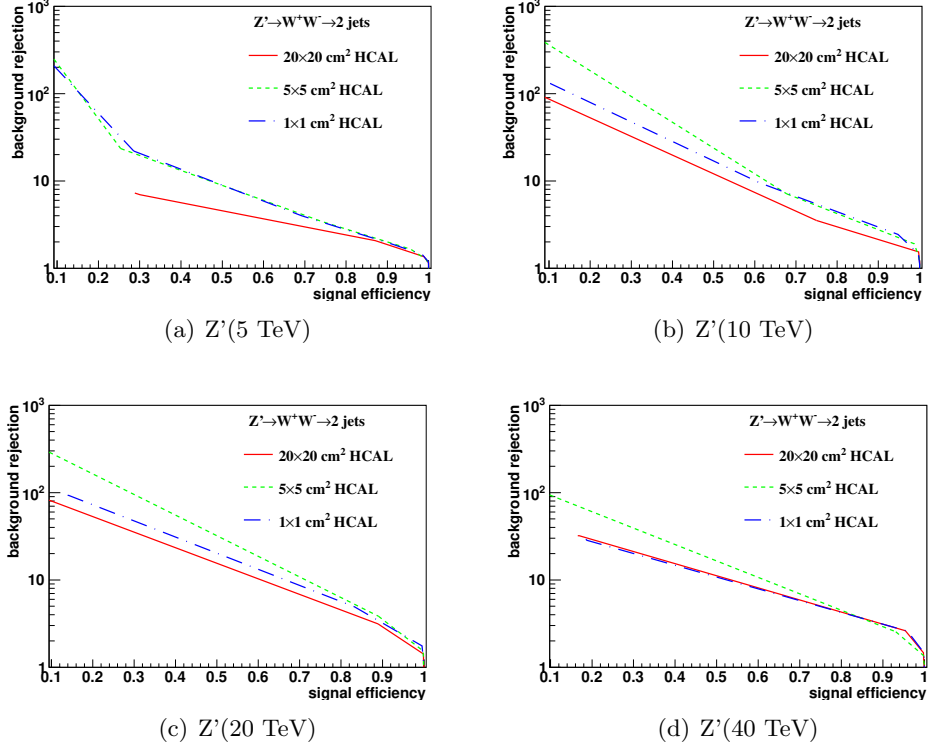


Figure 12: Signal efficiency versus background rejection rate using C_2^1 . The energies of collision at (a)5, (b)10, (c)20, (d)40TeV are shown here. In each picture, the three ROC curves correspond to different detector sizes.

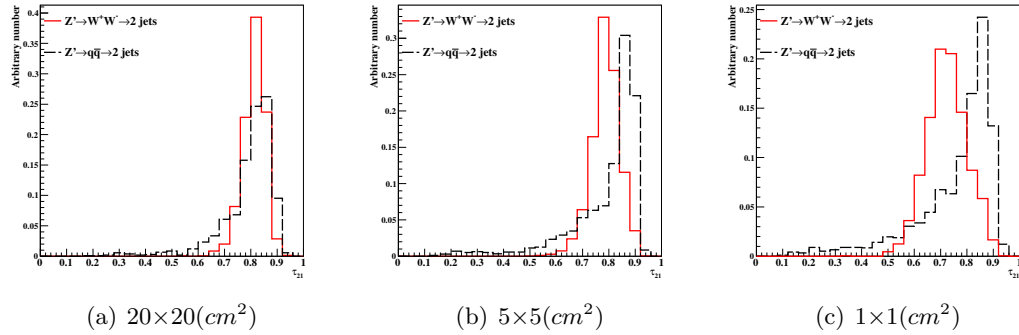


Figure 13: Distributions of Mann-Whitney value U in 20 TeV energy collision for τ_{21} in different detector sizes. Cell Size in 20×20 , 5×5 , and $1 \times 1 (cm \times cm)$ are shown here.

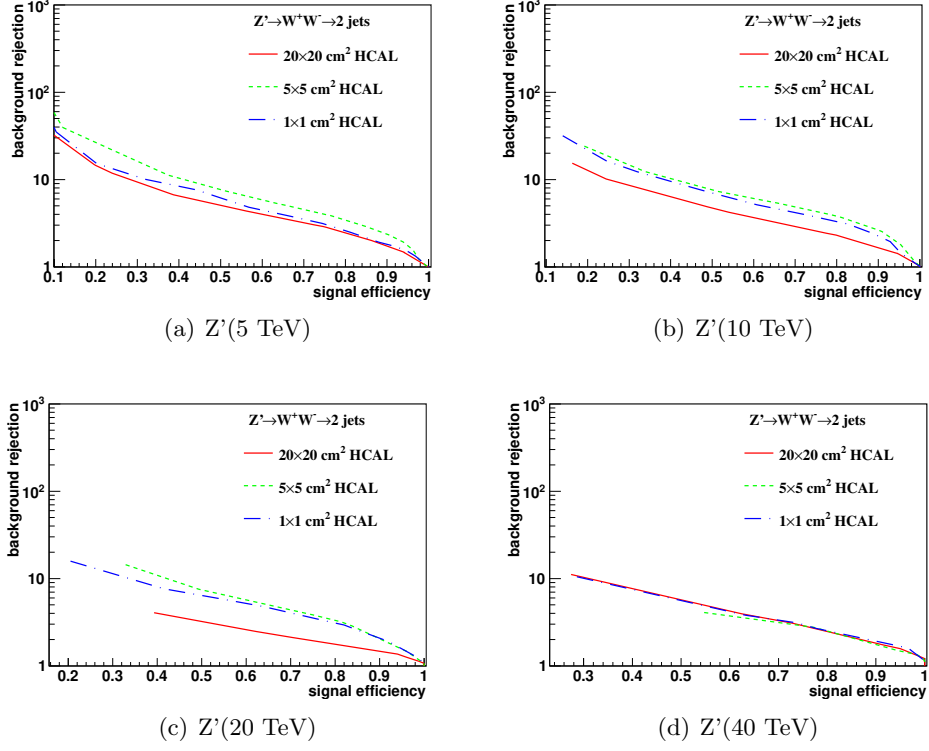


Figure 14: Signal efficiency versus background rejection rate using τ_{21} . The energies of collision at (a)5, (b)10, (c)20, (d)40TeV are shown here. In each picture, the three ROC curves correspond to different detector sizes.

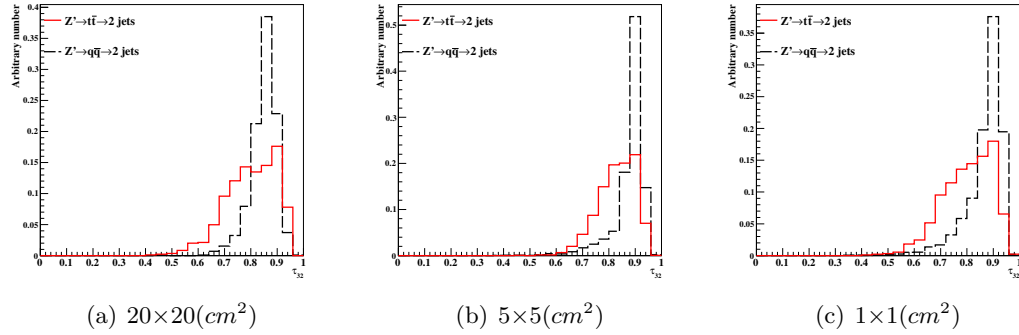


Figure 15: Distributions of Mann-Whitney value U in 20 TeV energy collision for τ_{32} in different detector sizes. Cell Size in 20×20 , 5×5 , and $1 \times 1 (cm \times cm)$ are shown here.

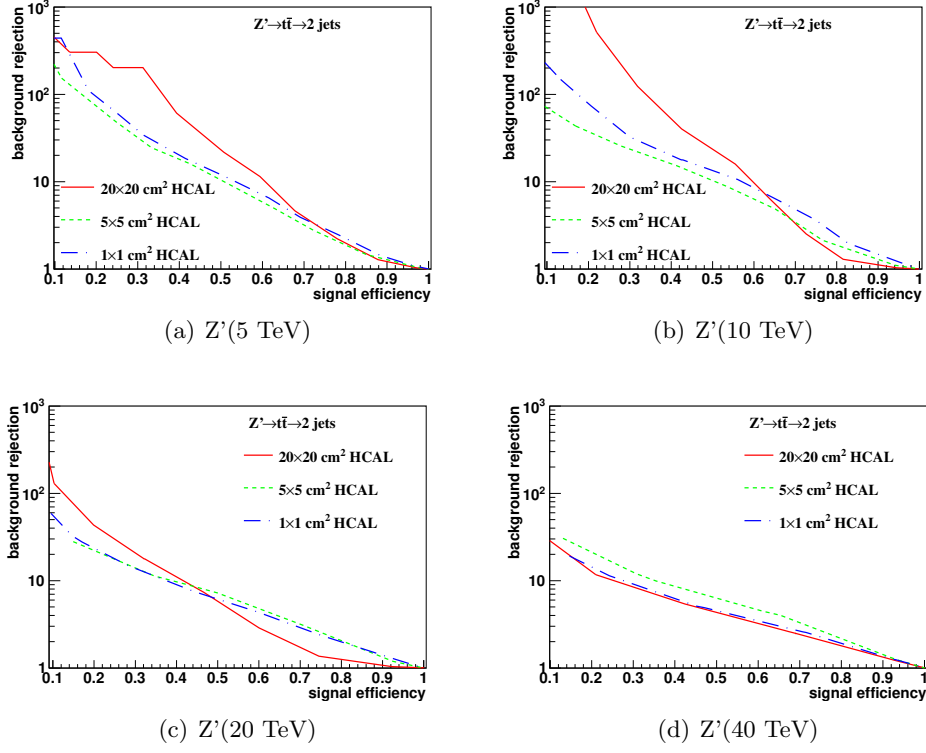


Figure 16: Signal efficiency versus background rejection rate using τ_{32} . The energies of collision at (a)5, (b)10, (c)20, (d)40TeV are shown here. In each picture, the three ROC curves correspond to different detector sizes.

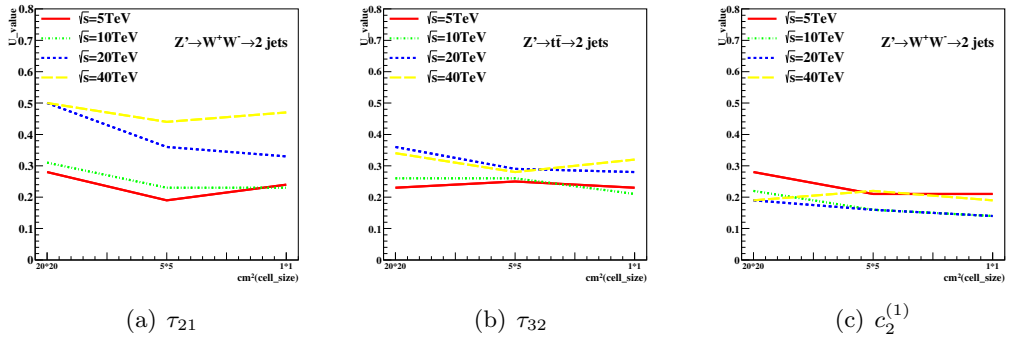


Figure 17: The Mann-Whitney U values for τ_{21}, τ_{32} and $c_2^{(1)}$ reconstructed from calorimeter hit at 05GeV cut with different collision energies correspond to different detector sizes in rawhit cut with 05GeV. The energies of collision at 5, 10, 20, 40, 20, 40TeV are shown in each figure.

References

- [1] M. Benedikt, [The Global Future Circular Colliders Effort](#) CERN-ACC-SLIDES-2016-0016. Presented at P5 Workshop on the Future of High Energy Physics, BNL, USA, Dec. 15-18, 2013. URL <http://cds.cern.ch/record/2206376>
- [2] J. Tang, et al., Concept for a Future Super Proton-Proton Collider (2015). [arXiv:1507.03224](#).
- [3] R. Calkins, et al., [Reconstructing top quarks at the upgraded LHC and at future accelerators](#), in: Proceedings, Community Summer Study 2013: Snowmass on the Mississippi (CSS2013): Minneapolis, MN, USA, July 29-August 6, 2013. [arXiv:1307.6908](#). URL <https://inspirehep.net/record/1244676/files/arXiv:1307.6908.pdf>
- [4] S. V. Chekanov, J. Dull, Energy range of hadronic calorimeter towers and cells for high-pT jets at a 100 TeV collider [arXiv:1511.01468](#).
- [5] E. Coleman, M. Freytsis, A. Hinzmann, M. Narain, J. Thaler, N. Tran, C. Vernieri, The importance of calorimetry for highly-boosted jet substructure [arXiv:1709.08705](#).
- [6] DELPHES 3 Collaboration, J. de Favereau, C. Delaere, P. Demin, A. Giammanco, V. Lematre, A. Mertens, M. Selvaggi, DELPHES 3, A modular framework for fast simulation of a generic collider experiment, JHEP 02 (2014) 057. [arXiv:1307.6346](#), [doi:10.1007/JHEP02\(2014\)057](#).
- [7] S. V. Chekanov, M. Beydler, A. V. Kotwal, L. Gray, S. Sen, N. V. Tran, S. S. Yu, J. Zuzelski, Initial performance studies of a general-purpose detector for multi-TeV physics at a 100 TeV pp collider, JINST 12 (06) (2017) P06009. [arXiv:1612.07291](#), [doi:10.1088/1748-0221/12/06/P06009](#).
- [8] J. Allison, et al., Recent developments in Geant4, Nuclear Instruments and Methods in Physics Research A 835 (2016) 186.
- [9] M. J. Charles, PFA Performance for SiD, in: Linear colliders. Proceedings, International Linear Collider Workshop, LCWS08, and International Linear Collider Meeting, ILC08, Chicago, USA, November 16-20, 2008 , 2009. [arXiv:0901.4670](#).
- [10] J. S. Marshall, M. A. Thomson, Pandora Particle Flow Algorithm, in: Proceedings, International Conference on Calorimetry for the High Energy Frontier (CHEF 2013), 2013, pp. 305–315. [arXiv:1308.4537](#).
- [11] G. P. S. M. Cacciari, G. Soyez, FastJet user manual CERN-PH-TH/2011-297. [arXiv:1111.6097](#).
- [12] M. Cacciari, G. P. Salam, G. Soyez, The anti-kt jet clustering algorithm, JHEP 0804 (2008) 063. [arXiv:0802.1189](#).
- [13] S. Chekanov, HepSim: a repository with predictions for high-energy physics experiments, Advances in High Energy Physics 2015 (2015) 136093, available as <http://atlaswww.hep.anl.gov/hepsim/>.
- [14] B. Auerbach, S. Chekanov, J. Love, J. Proudfoot, A. Kotwal, Sensitivity to new high-mass states decaying to ttbar at a 100 TeV collider [arXiv:1412.5951](#).
- [15] J. Butterworth, B. Cox, J. R. Forshaw, WW scattering at the CERN LHC, Phys.Rev. D65 (2002) 096014. [arXiv:hep-ph/0201098](#), [doi:10.1103/PhysRevD.65.096014](#).
- [16] S. Catani, Y. L. Dokshitzer, M. H. Seymour, B. R. Webber, [Longitudinally-invariant k-clustering algorithms for hadron-hadron collisions](#), Nuclear Physics B 406 (12) (1993) 187 – 224. URL <http://www.sciencedirect.com/science/article/pii/055032139390166M>
- [17] S. D. Ellis, D. E. Soper, Successive combination jet algorithm for hadron collisions, Phys. Rev. D48 (1993) 3160–3166. [arXiv:hep-ph/9305266](#), [doi:10.1103/PhysRevD.48.3160](#).
- [18] ATLAS Collaboration Collaboration, G. Aad, et al., Jet mass and substructure of inclusive jets in $\sqrt{s} = 7$ TeV pp collisions with the ATLAS experiment, JHEP 1205 (2012) 128. [arXiv:1203.4606](#), [doi:10.1007/JHEP05\(2012\)128](#).
- [19] J. Thaler, K. Van Tilburg, Identifying Boosted Objects with N-subjettiness, JHEP 03 (2011) 015. [arXiv:1011.2268](#), [doi:10.1007/JHEP03\(2011\)015](#).